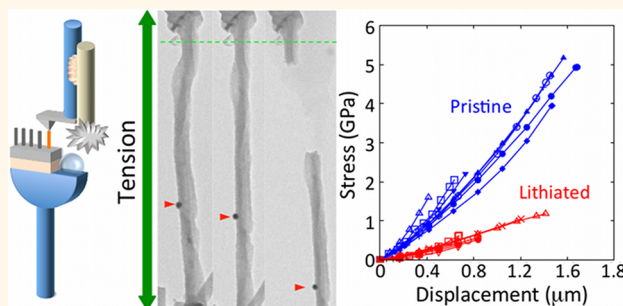# Quantitative Fracture Strength and Plasticity Measurements of Lithiated Silicon Nanowires by *In Situ* TEM Tensile Experiments

Akihiro Kushima,[†] Jian Yu Huang,[‡,*] and Ju Li[†,*]

[†]Department of Nuclear Science and Engineering and Department of Materials Science and Engineering, Massachusetts Institute of Technology, Cambridge, Massachusetts 02139, United States and [‡]Center for Integrated Nanotechnologies, Sandia National Laboratories, Albuquerque, New Mexico 87185, United States

Lithium-ion batteries (LIBs) are the leading power sources for electronics and electric vehicles. Nanostructured silicon (NS) anodes have attracted much attention for their high specific capacity (3579 mAh/g for $Li_{15}Si_4$) and some ability to accommodate large volume expansion (~300%).[1−3] However, a LIB with NS anode still shows capacity fading after multiple charge/discharge cycles.[1,4,5] Large compressive/tensile stresses repeat in the Si electrode during the battery cycles.[6] Unevenly distributed stress and nonuniform volume changes in the NS lead to its fracture and pulverization, causing loss of electrical contact and capacity.[1,4,7] Efforts are under way to overcome this problem by altering the nanostructures[8−11] or fabricating nanocomposites to buffer the large volume changes of the electrode during lithiation/delithiation.[1,4,7,12,13] To pursue an optimum design to stabilize the NS during battery operations, it is important to understand the mechanical property of silicon in lithiated states. There have been a number of experimental[14−18] and theoretical[19−25] works investigating the mechanical property of single-crystal Si nanowires (NWs). However, there is little work on measuring the mechanical properties of lithiated Si NWs. The *ex situ* indentation experiment conducted by Hertzberg *et al.* showed a significant decrease of the Young's modulus (by a factor of 7) for the lithiated Si thin film.[26] However, the direct observation of fracture, which is important for understanding the NW electrode degradation, is still missing. In this work we present for the first time an *in situ* method that allows for seamless transition from the lithiation experiment of NWs to their mechanical

ABSTRACT

We report *in situ* tensile strength measurement of fully lithiated Si (Li—Si alloy) nanowires inside a transmission electron microscope. A specially designed dual probe with an atomic force microscopy cantilever and a scanning tunneling microscopy electrode was used to conduct lithiation of Si nanowires and then perform *in situ* tension of the lithiated nanowires. The axial tensile strength decreased from the initial value of 3.6 GPa for the pristine unlithiated Si nanowires to 0.72 GPa for the lithiated Li—Si alloy. We observed large fracture strain ranging from 8% to 16% for Li—Si alloy, 70% of which remained permanent after fracture. This indicates a certain degree of tensile plasticity in the lithiated silicon before fracture, important for constitutive modeling of the lithium-ion battery cyclability. We also compare the *ab initio* computed ideal strengths with our measured strengths and attribute the differences to the morphology and flaws in the lithiated nanowires.

KEYWORDS: constitutive law · battery cyclability · bending · apparent strain *vs* true strain · ideal strength

strength testing inside a transmission electron microscope (TEM).

RESULTS AND DISCUSSION

A schematic of the experimental setup using a Nanofactory TEM—scanning tunneling microscopy (STM) holder with a 3D piezoelectric manipulator is shown in Figure 1A. On the manipulator side (left in Figure.1A), a tip-flattened Al rod was mounted. A tiny piece of Si wafer with Si NWs grown on it was
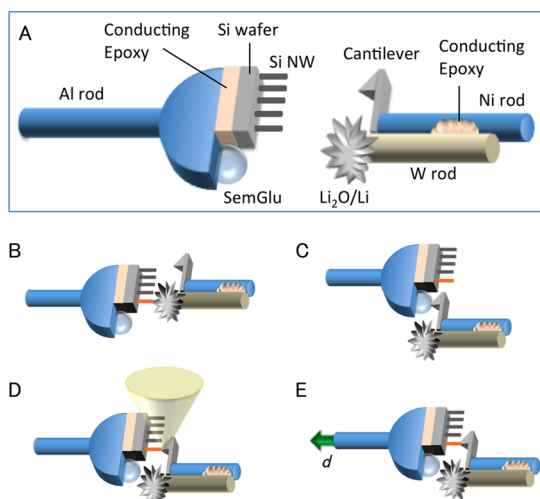
Figure 1. (A) Schematic illustration of the experimental setup. A tiny piece of Si wafer with the [111] oriented NWs was glued to the tip-flattened Al rod using a conducting epoxy. The Al rod was connected to the 3D-piezoelectric manipulator. A small amount of SemGlu was attached to the side of the Al rod. A Ni rod with a Si AFM cantilever glued to the tip was mounted to the other side of the holder. The W rod with scratched Li was also glued to the Ni rod. (B–E) Experimental procedure of the lithiation and the *in situ* tension of the NW. (B) A Si NW was lithiated using the Li metal as the counter electrode. (C) The Al rod was manipulated to contact the SemGlu with the tip of the AFM cantilever. (D) The Al rod was manipulated to contact the lithiated Si NW with the AFM cantilever. (E) Finally, the tensile stress was applied to the NW by a displacement-controlled piezo movement at a rate of 1–5 nm/s.

attached to the Al rod by a conducting epoxy. A small amount of SemGlu (Kleindiek Nanotechnik) was also placed on the front of the rod. On the other side of the holder, a Ni rod with a Si atomic force microscopy (AFM) cantilever (Nanosensors, PPP-NCHR-20) on the tip was connected. The spring constant of the cantilever was 30 N/m. The W rod was bound to the Ni rod with a conducting epoxy. Fresh Li metal was loaded on the tip of the W rod inside a glovebox. The TEM holder was placed in a plastic bag in an argon-filled glovebox and transferred to the TEM to minimize the air exposure of the Li.

The experimental procedure is explained in Figure 1B–E. First a Si NW was contacted with the Li_2O on the surface of the Li metal, and a -4.0 V potential was applied to the NW with respect to the Li for lithiation (Figure 1B).[3] Once the NW was lithiated, the AFM cantilever was manipulated to contact the SemGlu, and a small portion of the SemGlu was transferred to the tip of the AFM cantilever (Figure 1C). Here we use the electron beam at low dose ($<5.0 \times 10^{-4}$ A/cm^2) to prevent the glue from solidifying. Then, the cantilever was manipulated to contact the lithiated NW, and the electron beam was focused at the contact point to cure the glue (Figure 1D). Finally, tensile stress was applied to the NW by a controlled displacement d (1–5 nm/s) to pull

the Si nanowire away from the cantilever (Figure 1E). The force acting on the NW was obtained by measuring the displacement of the cantilever. The displacement and elongation of the NW were directly measured from the TEM images.

Figure 2A–E shows the deformation of the lithiated Si NW under axial tension (see also Supplementary Movie M1). The electron diffraction pattern of the NW after the lithiation clearly indicates that the NW was fully lithiated to the $Li_{15}Si_4$ phase (see also Supplementary Figure S1 for the high-resolution image).[3] A feature on the upper part of the NW is aligned on the dashed line in the figure. The tensile strain was evaluated by calculating the distance between the upper mark and another feature at the lower part of the NW indicated by the arrowhead. As we pulled the NW, the NW was elongated as shown in Figure 1B–D until it was fractured (Figure 1E). We confirmed from the fracture surface that there was no unreacted Si core inside the NW (Figure 1F). The figure shows the NW was porous after the fracture. There could be two reasons for the porosity: (1) void nucleation during mechanical loading and (2) partial delithiation of the NW during tension. Since SemGlu is a nonconducting glue, the delithiation could be due to the electron beam effect, which we observed when the lithiated Si NW was exposed to a high-intensity electron beam (see Supplementary Figure S2). The growth of Li flakes was observed under the electron-beam-induced delithiation. During the tension, we reduced the beam intensity so that the Li flakes did not grow while imaging, and the flakes were not observed at or near the fracture surface. Thus there should be little to no effect of the electron beam on the porosity.

We followed the same procedure and conducted the tensile experiments for six lithiated Si NWs. The cross-sectional area of the fracture surface was used to evaluate the stress acting on the nanowire. Here, we assumed a circular cross-section. The force was calculated by measuring the displacement of the cantilever during the tension. The measured engineering stress–strain curves of the lithiated Si NWs are shown in Figure 3. The variation in the curves is due to the unevenly curved nature of the lithiated NWs. Every NW had its own unique curved shape after lithiation (see Supplementary Movies M2 and M3). Although some NWs had an unreacted Si core, we confirmed that the core is not present near the fracture point (see Supplementary Figure S3). The apparent strain of a NW is defined by the change in the length of the segment between two distinctive features in the NW as described above. We selected the segment so that there would be little (<5% of the cross section area) to no unreacted Si core, and the effect of the core on the stress–strain relationships is expected to be minimal. Although the presence of the core could be a contributing factor for the variation of the curves, the
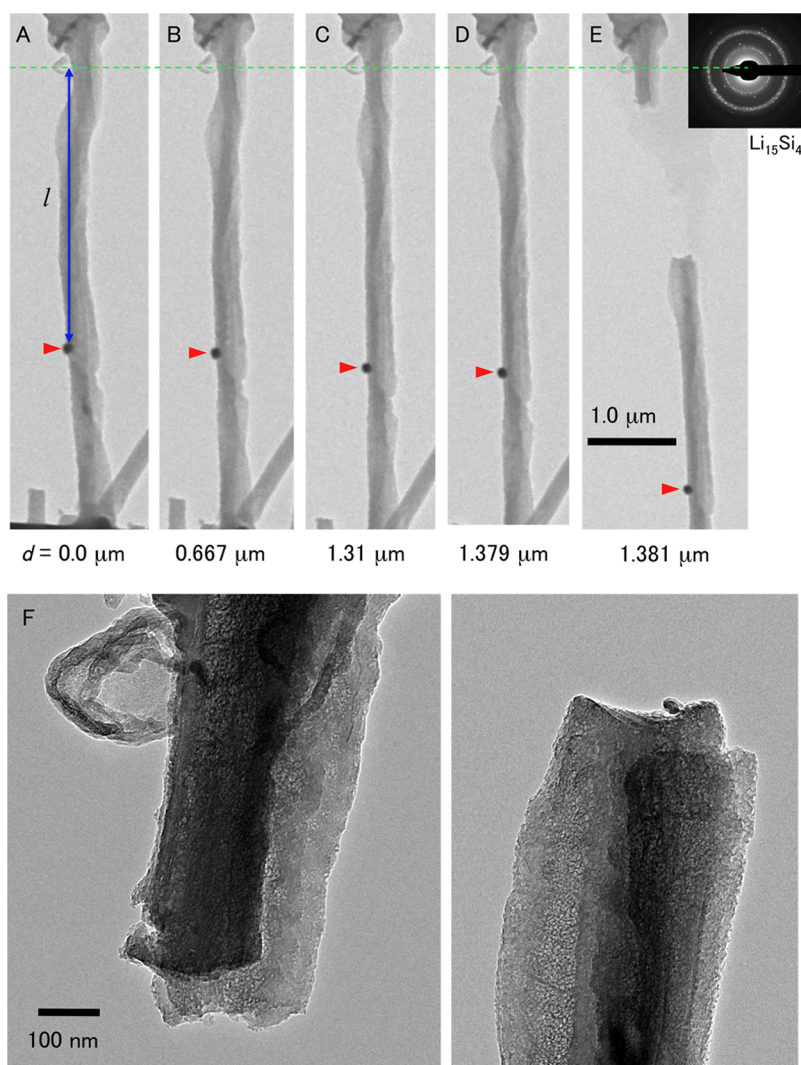
Figure 2. (A−E) *In situ* tensile deformation of the lithiated Si NW. The inset is the electron diffraction pattern of the NW, indicating the NW was fully lithiated to the $Li_{15}Si_4$ phase. The NW in the figure is aligned to a feature on the upper part of the NW, as marked by the dashed line. The tensile strain is defined by the change in the distance between the feature on the dashed line and the feature marked by the arrowheads. (F) Fracture surface of the NW showing no sign of the unreacted Si core.

effect is to overestimate the modulus. The average Young's modulus of the lithiated NWs was 2.4−12 GPa (7.9 GPa on average), which is much smaller than 180 GPa of the single crystal Si in [111] tension. Although a significant reduction in the Young's modulus was observed for the Si NWs with a diameter less than 30 nm,[17] the size of the Si NWs used in this work is large enough (∼130 nm in diameter) and the size effect on the mechanical property should be negligible. Thus, the significant reduction in the Young's modulus is an outcome of the lithiation. The value obtained in this work agrees with the reported value of 12 GPa for the $Li_{15}Si_4$ thin film.[26] The average strain at fracture was 10%. We note here that the measured 10% is the *apparent* tensile strain at failure, which because of the unbending (straightening) of the initially wavy nanowire may be somewhat larger than the true tensile strain: imagine for the sake of argument the stretching of an elastic spring, where the apparent

strain can greatly exceed the true strain at a solid material element level due to bending. Visual examinations (see Supplementary Movies M1−M3) though show that significant true tensile strains did occur, and the unbending should account for less than half of the apparent strain. The apparent stress−strain relationships at and after the fracture are connected by the dashed line in Figure 3. The results indicate that there exists a permanent plastic strain after the fracture. The ratio of the plasticity was approximately 70% of the total strain for all the lithiated Si NWs investigated, which can also be seen by watching marker motions in the Supplementary Movies M1−M3.

Since we evaluated the *apparent* strain, the measured plasticity includes unbending of the NWs. The actual plasticity may be larger or smaller than the above estimated 70% depending of the location in the NWs because the strain may be distributed non-uniformly in the NW. Figure 4 shows the stress−strain

curves evaluated by the change in the lengths of the different segments within a lithiated NW. The data show highest strain for the shortest segment near the bent point, indicating the strain was concentrated at the local region. However, the degree of the plasticity ranged from 60% to 80%, which is close to the average plasticity calculated, indicating the plasticity was nearly uniformly distributed in the NW regardless of the difference in the local strain. This is a significant piece of information because the extent to which plastic flow can happen in lithiated silicon is important for constitutive modeling of the battery cyclability.

Next, we compare the fracture strength of the lithiated Si NWs with the pristine ones. The tensile strength of the pristine Si NW was tested using the
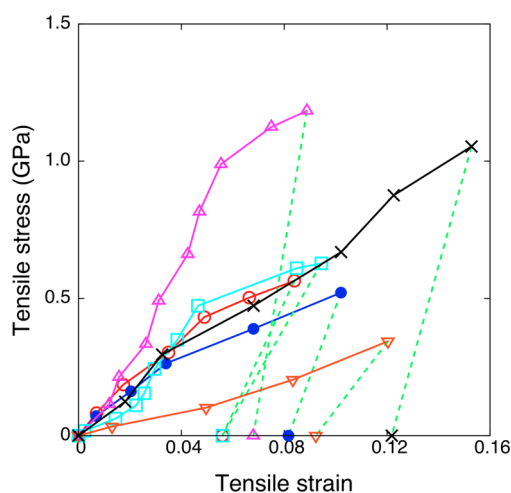

Figure 3. Tensile stress−strain curves of the lithiated Si NWs. The average Young's modulus, fracture stress, and the strain were 7.9 GPa, 0.72 GPa, and 10%, respectively. The dashed lines connect the fracture point and the residual strain after the fracture. The plastic strain was ∼7%.

platform as shown in Figure 1. Since the fracture strain of the Si NW is low (2−5% for the size of the NWs used in this work)[18] and the axes of the NWs were not perfectly aligned with the tensile direction in this experiment, the strain of the pristine Si NWs cannot be measured precisely due to larger experimental error. However, accurate evaluation of the stress is possible by observing the displacement of the cantilever.

The data of the pristine Si (Figure 5A) are concaved upward because the NWs were initially tilted away from the tensile direction. As the wafer was displaced away from the cantilever, the axis of the Si NW bent and became more closely aligned with the tensile direction, causing the increase of the resistance against tension. The strengths of the NWs are summarized in Figure 5B. The average tensile strength of the pristine NWs was 3.6 GPa, which agrees well with other experimental data.[14] This validates our method for the tensile strength evaluation of the NWs. The strength of the lithiated NWs is reduced to 0.72 GPa, which is 20% of that of the pristine NWs.

We also conducted quantum mechanical *ab initio* calculations of tensile deformation of the lithiated and the pristine Si to understand the difference in their mechanical properties. Figure 6A shows the computed stress−strain curves for the single-crystal Si and $Li_{15}Si_4$ under periodic boundary conditions. The tensile strain was applied along [111] for Si and [001] for $Li_{15}Si_4$. The calculated Young's modulus, the fracture stress, and the strain are 173 GPa, 19.3 GPa, and 18% for the single-crystal Si and 33.5 GPa, 6.54 GPa, and 28% for $Li_{15}Si_4$. The softening of the elastic modulus and the weakening of the failure strength of the lithiated Si agree with our experimental observations. However, the absolute magnitudes of the failure stress differ by a factor of 5−9 for lithiated and unlithiated silicon. Such a difference between calculated ideal strength and the actual
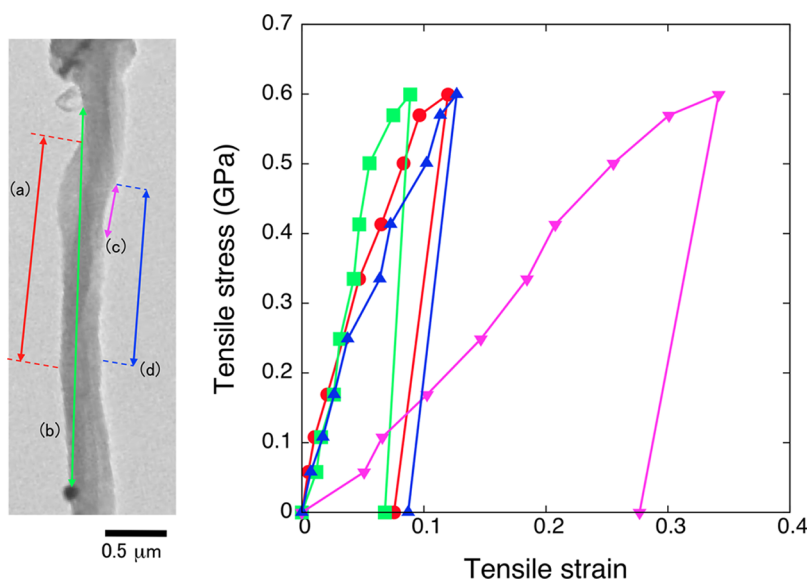

Figure 4. Stress−strain curve of a lithiated Si NW using the strain measured at different segments in the NW. Circles, squares, down triangles, and up triangles are the results using the strain of the segments (a), (b), (c), and (d), respectively.
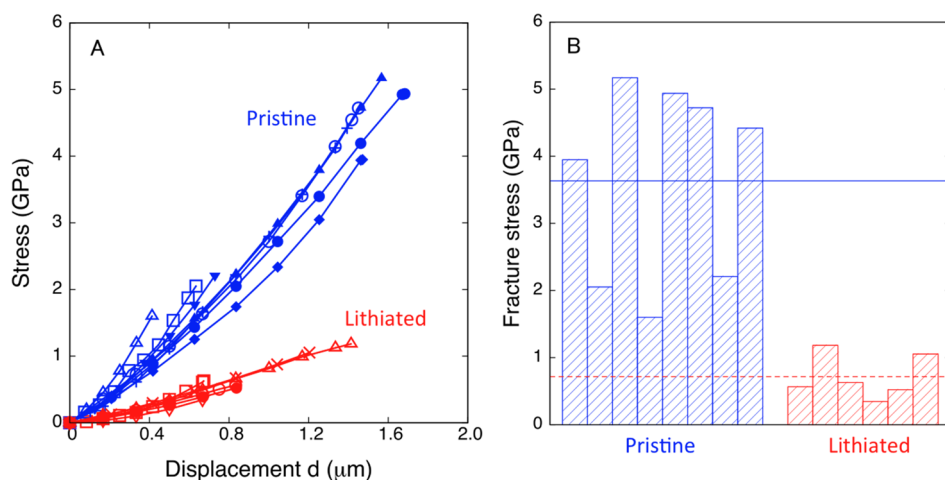
Figure 5. (A) Stress-displacement plot of the lithiated NWs. The blue and red lines are data from the pristine and the lithiated Si NWs, respectively. (B) Fracture strength of the pristine Si NW and the $Li_{15}Si_4$ NW. The solid and dashed lines indicate the average fracture strength of the pristine (3.6 GPa) and the lithiated (0.72 GPa) NWs, respectively.

measured strength is quite common.[27] First, the calculated Figure 6A has no effects of temperature. Without the aid of thermal fluctuations, it requires higher stress to break or switch bonds athermally. Second, the calculated Figure 6A has no effects of pre-existing defects or flaws (microstructure) that would lower the stress for bond breaking. One of these defects could be the free surface. We note that in the context of utilizing nanostructured silicon for engineering applications, there are plenty of free surfaces, which are preferential sites for crack initiation. In this sense, the computed *ab initio* bulk ideal strengths in Figure 6A are indeed too "idealistic", and our quantitatively measured NW tensile strengths should much more closely match the reality (finite temperature, laboratory strain rates, realistic surfaces, realistic nanostructure size scale including possible internal pores) in an engineering setting and, therefore, can be directly used for fitting the constitutive law for lithiated silicon.

Nonetheless, the computed *ab initio* bulk ideal strengths give useful insights for understanding bonding patterns and deformation physics in the bulk. The change in the atomic structures and the charge density distributions of the single-crystal Si and the $Li_{15}Si_4$ are shown in Figure 6B and C, respectively. The iso-surface in the figure corresponds to the value of 0.3 $Å^{-3}$. In the single-crystal Si, electrons are localized between Si atoms, forming covalent bonds. The Si–Si bonds along the tensile direction were stretched during tension, leading to a decrease in the charge density between the atoms. The bond A–B in the figure was 2.37 Å at equilibrium. It was elongated to 2.78 Å at a strain of 18%, where the maximum strain was observed. At the fracture, the bonds were broken, as indicated by the dashed line in the figure, and the bond A–B recovered the original length of 2.37 Å. This indicates that the brittle fracture took place in the single-crystal Si with no plasticity.

On the other hand, Si atoms were isolated in $Li_{15}Si_4$ with Li atoms filling the space between them, and most of the electrons were localized around the Si atoms. Due to the absence of covalent Si–Si bonds and the presence of weak ionic Li–Si and metallic Li–Li bonds, $Li_{15}Si_4$ showed a much lower Young's modulus than the single-crystal Si.[28] Additionally, the shear-weak, metallic-like bonding allowed the atoms in $Li_{15}Si_4$ to move more freely and enabled $Li_{15}Si_4$ to accommodate larger plastic strain compared to the single-crystal Si.[29] In our quantum mechanical calculation, $Li_{15}Si_4$ can undergo up to 70% strain, at which point a large stress drop occurred. At this point, the formation of a void indicated by the dashed circle was observed following a large rearrangement of the atoms. The void formation under tension agrees with the experimental observation of the NW becoming porous after the fracture, as shown in Figure 2F. If the tensile stress was removed, the calculated supercell would not relax back to its original shape, and 52% strain remains as a permanent plastic strain, indicating plenty of bond-switching processes had already happened prior to complete decohesion. Unlike the single-crystal Si, where bond-switching was highly restricted due to covalent bonding, the atoms in $Li_{15}Si_4$ could freely rearrange to accommodate a large deformation. After the rearrangements took place, the atoms in the system lost the memory of the original positions (plasticity) because of the complex structural change. This was not the case in the Si single crystal, where decohesion happened before much bond-switching took place.

CONCLUSION

In summary, we developed an *in situ* TEM technique to measure the tensile strength of the NWs before and after lithiation. The lithiated Si NW has a much smaller Young's modulus and tensile strength compared to the pristine Si NWs at room temperature. The results also
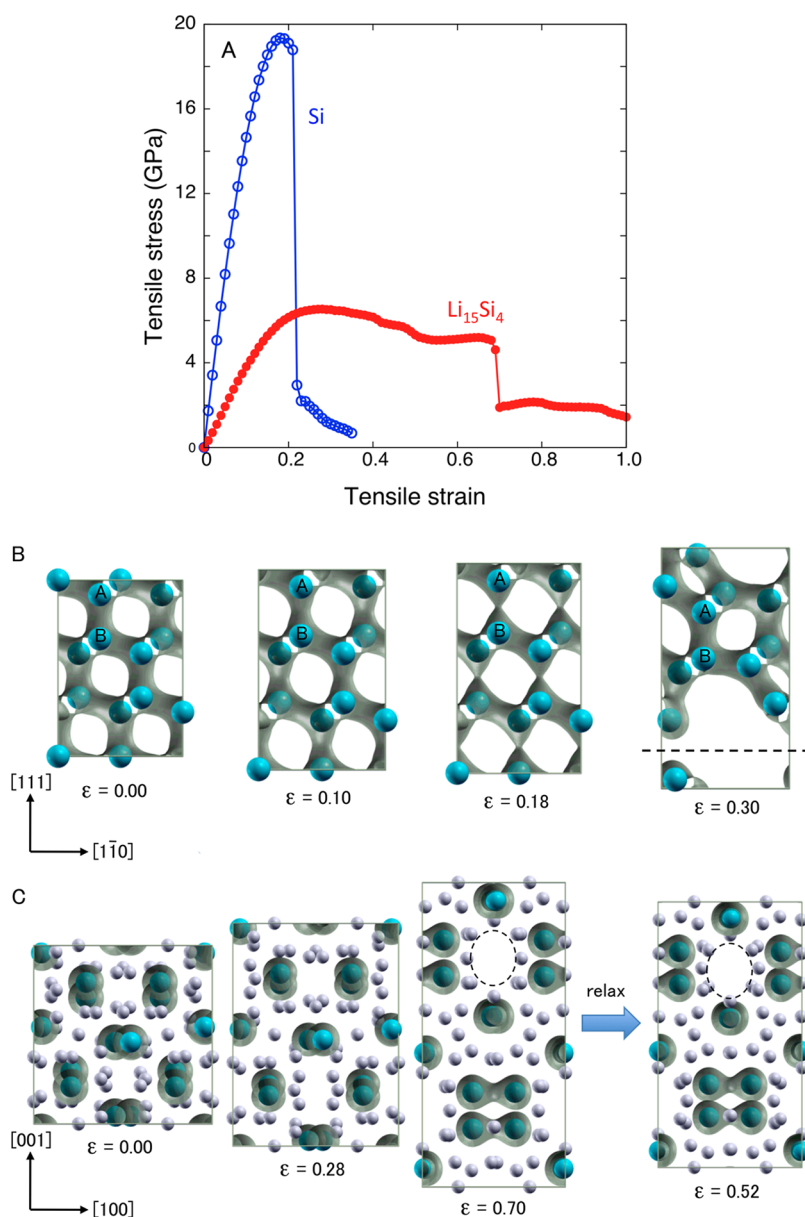
Figure 6. (A) Ideal tensile stress−strain curves of single-crystal Si and Li$_{15}$Si$_4$ from quantum mechanical *ab initio* calculation. (B) Change in the atomic and the electronic structures of the single-crystal Si during tension. (C) Change in the atomic and the electronic structures of the Li$_{15}$Si$_4$ during tension. The iso-surface in the figure is 0.3 electron/Å^3.

revealed a large permanent plastic strain after the fracture, which was not seen in the pristine Si NWs. Our measurements complement the indentation experiment by Hertzberg *et al.*[26] in two aspects: (a) Hertzberg *et al.*'s measurements were *ex situ*, whereas ours were *in situ* inside the TEM, and (b) indentation experiments mostly interrogate material behavior under compression, whereas our experiment is simple tension-dominated. Since the silicon anode experiences both compression and tension during cycling,

and failure happens often in tension, our experimental measurements bring valuable information for constitutive modeling of nanostructured silicon for lithium-ion battery anodes. Although this experimental method is demonstrated here for the Si NWs, it is not limited to Si and can be applied straightforwardly to all kinds of NWs. The technique presented in this work can thus provide useful information for creating robust nanostructured electrode materials for high-performance Li-ion batteries.

METHODS

Si NW Fabrication. The Si NWs used in the experiment were grown on a heavily doped Si(111) wafer (n-type, $\rho = 0.001\ \Omega4\cdot$cm)

via the vapor−liquid−solid mechanism catalyzed by 100 nm Au nanoparticles. SiCl$_4$ (600 Torr, diluted in H$_2$/N$_2$) was introduced into a CVD furnace, and the red phosphorus powder was used as the dopant source. Epitaxial Si NWs with [111] growth direction,

lengths ~6 μm, and diameters ~130 nm were obtained from a 4 min growth at 900 °C.

Ab Initio Simulation. For Si single crystals, a 3.87 Å × 6.70 Å × 9.47 Å unit cell including 12 atoms was used. The crystallographic orientations of the simulation cell are [1$\bar{1}$0], [11$\bar{2}$], and [111] in the *x*, *y*, and, *z* direction, respectively. We employed a density functional theory formalism with generalized gradient approximation parametrized by Perdew, Burke, and Ernzerhof[30] using a planewave basis set. The ionic cores were represented with projector-augmented wave potentials.[31,32] An energy cutoff of 400 eV was chosen for the expansion of the plane wave function, and a 10 × 6 × 4 Monkhorst−Pack[33] *k*-point mesh was selected in the simulations. First, the atomic configurations and the cell vectors were relaxed to minimize the total energy of the system. Then the tensile strain was applied to the model by elongating the simulation cell along the *z* direction with an increment of 0.01. After each increment of the strain, the structural optimization was performed while fixing the cell size in the *z* direction. For $Li_{15}Si_4$, a 10.6 Å × 10.6 Å × 10.6 Å unit cell of the *I*43*d* space group lattice including 60 Li and 16 Si atoms was used. The crystallographic orientations of the simulation cell are [100], [010], and [001] in the *x*, *y*, and, *z* direction, respectively. A 4 × 4 × 4 Monkhorst−Pack[4] *k*-point mesh was selected in the simulations. All other conditions were the same as in the simulation of the single-crystal Si.

Conflict of Interest: The authors declare no competing financial interest.

Supporting Information Available: High-resolution image of the Si NW before and after the lithiation, electron beam induced delithiation of the lithiated Si NW, the fracture surface and the unreacted Si core of the lithiated Si NW, and *in situ* TEM movies showing the tensile deformation process of the lithiated Si NWs. This material is available free of charge *via* the Internet at http://pubs.acs.org.

REFERENCES AND NOTES

1. Chan, C. K.; Peng, H.; Liu, G.; McIlwrath, K.; Zhang, X. F.; Huggins, R. A.; Cui, Y. High-Performance Lithium Battery Anodes Using Silicon Nanowires. *Nat. Nanotechnol.* **2008**, *3*, 31–35.
2. Liu, X. H.; Zhang, L. Q.; Zhong, L.; Liu, Y.; Zheng, H.; Wang, J. W.; Cho, J.-H.; Dayeh, S. A.; Picraux, S. T.; Sullivan, J. P.; *et al.* Ultrafast Electrochemical Lithiation of Individual Si Nanowire Anodes. *Nano Lett.* **2012**, *11*, 2251–2258.
3. Liu, X. H.; Zheng, H.; Zhong, L.; Huang, S.; Karki, K.; Zhang, L. Q.; Liu, Y.; Kushima, A.; Liang, W. T.; Wang, J. W.; *et al.* Anisotropic Swelling and Fracture of Silicon Nanowires during Lithiation. *Nano Lett.* **2012**, *11*, 3312–3318.
4. Huang, R.; Fan, X.; Shen, W.; Zhu, J. Carbon-Coated Silicon Nanowire Array Films for High-Performance Lithium-Ion Battery Anodes. *Appl. Phys. Lett.* **2009**, *95*, 133119.
5. Szczech, J. R.; Jin, S. Nanostructured Silicon for High Capacity Lithium Battery Anodes. *Energy Environ. Sci.* **2011**, *4*, 56.
6. Sethuraman, V. A.; Chon, M. J.; Shimshak, M.; Srinivasan, V.; Guduru, P. R. *In Situ* Measurements of Stress Evolution in Silicon Thin Films during Electrochemical Lithiation and Delithiation. *J. Power Sources* **2011**, *195*, 5062.
7. Kim, H.; Cho, J. Superior Lithium Electroactive Mesoporous Si@Carbon Core−Shell Nanowires for Lithium Battery Anode Material. *Nano Lett.* **2008**, *8*, 3688–3691.
8. Magasinski, A.; Dixon, P.; Hertzberg, B.; Kvit, A.; Ayala, J.; Yushin, G. High-Performance Lithium-Ion Anodes Using a Hierarchical Bottom-Up Approach. *Nat. Mater.* **2010**, *9*, 353–358.
9. Hu, L.; Wu, H.; Hong, S. S.; Cui, L.; McDonough, J. R.; Bohy, S.; Cui, Y. Si Nanoparticle-Decorated Si Nanowire Networks for Li-Ion Battery Anodes. *Chem. Commun.* **2011**, *47*, 367.
10. Nguyen, H. T.; Yao, F.; Zamfir, M. R.; Biswas, C.; So, K. P.; Lee, Y. H.; Kim, S. M.; Cha, S. N.; Kim, J. M.; Pribat, D. Highly Interconnected Si Nanowires for Improved Stability Li-Ion Battery Anodes. *Adv. Energy Mater.* **2011**, *1*, 1154–1161.
11. Cui, L.-F.; Ruffo, R.; Chan, C. K.; Peng, H.; Cui, Y. Crystalline-Amorphous Core−Shell Silicon Nanowires for High Capacity and High Current Battery Electrodes. *Nano Lett.* **2009**, *9*, 491–495.
12. Cui, L.-F.; Yang, Y.; Hsu, C.-M.; Cui, Y. Carbon−Silicon Core−Shell Nanowires as High Capacity Electrode for Lithium Ion Batteries. *Nano Lett.* **2009**, *9*, 3370–3374.
13. Zang, J.-L.; Zhao, Y.-P. Silicon Nanowire Reinforced by Single-Walled Carbon Nanotube and Its Applications to Anti-Pulverization Electrode in Lithium Ion Battery. *Composites, Part B* **2012**, *43*, 76–82.
14. Kim, Y.; Son, K.; Choi, I.; Choi, I.; Park, W. I.; Jang, J. Exploring Nanomechanical Behavior of Silicon Nanowires: AFM Bending *versus* Nanoindentation. *Adv. Funct. Mater.* **2011**, *21*, 279–286.
15. Sethuraman, V. A.; Srinivasan, V.; Bower, A. F.; Guduru, P. R. *In Situ* Measurements of Stress-Potential Coupling in Lithiated Silicon. *J. Electrochem. Soc.* **2010**, *157*, A1253.
16. Sohn, Y.-S.; Park, J.; Yoon, G.; Song, J.; Jee, S.-W.; Lee, J.-H.; Na, S.; Kwon, T.; Eom, K. Mechanical Properties of Silicon Nanowires. *Nanoscale Res. Lett.* **2009**, *5*, 211–216.
17. Zhu, Y.; Xu, F.; Qin, Q.; Fung, W. Y.; Lu, W. Mechanical Properties of Vapor−Liquid−Solid Synthesized Silicon Nanowires. *Nano Lett.* **2012**, *9*, 3934–3939.
18. Passi, V.; Bhaskar, U.; Pardoen, T.; Sodervall, U.; Nilsson, B.; Petersson, G.; Hagberg, M.; Raskin, J.-P. Note: Fast and Reliable Fracture Strain Extraction Technique Applied to Silicon at Nanometer Scale. *Rev. Sci. Instrum.* **2011**, *82*, 116106.
19. Leu, P. W.; Svizhenko, A.; Cho, K. Ab Initio Calculations of the Mechanical and Electronic Properties of Strained Si Nanowires. *Phys. Rev. B* **2008**, *77*, 235305.
20. Furmanchuk, A.; Isayev, O.; Dinadayalane, T. C.; Leszczynski, J. Car−Parrinello Molecular Dynamics Simulations of Tensile Tests on Si⟨001⟩ Nanowires. *J. Phys. Chem. C* **2012**, *115*, 12283–12292.
21. Lee, B.; Rudd, R. E. First-Principles Calculation of Mechanical Properties of Si⟨001⟩ Nanowires and Comparison to Nanomechanical Theory. *Phys. Rev. B* **2007**, *75*, 195328.
22. Kim, H.; Tomar, V. Nanometer to Micron Scale Mechanics of [100] Silicon Nanowires Using Atomistic Simulations at Accelerated Time Steps. *Phys. Status Solidi A* **2011**, *208*, 2115–2123.
23. Yang, Z.; Lu, Z.; Zhao, Y.-P. Shape Effects on the Yield Stress and Deformation of Silicon Nanowires: A Molecular Dynamics Simulation. *J. Appl. Phys.* **2009**, *106*, 023537.
24. Kang, K.; Cai, W. Size and Temperature Effects on the Fracture Mechanisms of Silicon Nanowires: Molecular Dynamics Simulations. *Int. J. Plast.* **2010**, *26*, 1387–1401.
25. Lee, B.; Rudd, R. E. Size-Dependent Si Nanowire Mechanics Are Invariant to Changes in the Surface State. *Phys. Rev. B* **2011**, *84*, 161303.
26. Hertzberg, B.; Benson, J.; Yushin, G. *Ex-Situ* Depth-Sensing Indentation Measurements of Electrochemically Produced Si−Li Alloy Films. *Electrochem. Commun.* **2011**, *13*, 818–821.
27. Zhu, T.; Li, J. Ultra-Strength Materials. *Prog. Mater. Sci.* **2010**, *55*, 710–757.
28. Shenoy, V. B.; Johari, P.; Qi, Y. Elastic Softening of Amorphous and Crystalline Li−Si Phases with Increasing Li

Concentration: A First-Principles Study. *J. Power Sources* **2010**, *195*, 6825–6830.

29. Zhao, K.; Wang, W. L.; Gregoire, J.; Pharr, M.; Suo, Z.; Vlassak, J. J.; Kaxiras, E. Lithium-Assisted Plastic Deformation of Silicon Electrodes in Lithium-Ion Batteries: A First-Principles Theoretical Study. *Nano Lett.* **2011**, *11*, 2962–2967.

30. Perdew, J. P.; Burke, K.; Ernzerhof, M. Generalized Gradient Approximation Made Simple. *Phys. Rev. Lett.* **1996**, *77*, 3865.

31. Kresse, G.; Joubert, D. From Ultrasoft Pseudopotentials to the Projector Augmented-Wave Method. *Phys. Rev. B* **1999**, *59*, 1758.

32. Blöchl, P. E. Projector Augmented-Wave Method. *Phys. Rev. B* **1994**, *50*, 17953.

33. Monkhorst, H. J.; Pack, J. D. Special Points for Brillouin-Zone Integrations. *Phys. Rev. B* **1976**, *13*, 5188.